Title

Frequency Domain Green's Function for a Planar Periodic Semi-infinite Phased Array. Part II: Phenomenology of the Diffracted waves

Permalink

https://escholarship.org/uc/item/27k8d3cc

Journal

IEEE Trans. Antennas and Propagation, 48(1)

Authors

Capolino, F
Capolino, F
Albani, M
et al.

Publication Date

2000

Copyright Information

This work is made available under the terms of a Creative Commons Attribution License, availalbe at https://creativecommons.org/licenses/by/4.0/

Peer reviewed

Frequency-Domain Green's Function for a Planar Periodic Semi-Infinite Phased Array—Part II: Diffracted Wave Phenomenology

F. Capolino, *Member, IEEE*, M. Albani, *Student Member, IEEE*, S. Maci, *Senior Member, IEEE*, and L. B. Felsen, *Life Fellow, IEEE*

Abstract—This second part of a two-paper sequence deals with the physical interpretation of the rigorously derived high-frequency asymptotic wave-field solution in Part I, pertaining to a semi-infinite phased array of parallel dipole radiators. The asymptotic solution contains two parts that represent contributions due to truncated Floquet waves (FW's) and to the corresponding edge diffractions, respectively. The phenomenology of the FW-excited diffracted fields is discussed in detail. All possible combinations of propagating (radiating) and evanescent (nonradiating) FW and diffracted contributions are considered. The format is a generalization of the conventional geometrical theory of diffraction (GTD) for smooth truncated aperture distributions to the truncated periodicity-induced FW distributions with their corresponding FW-modulated edge diffractions. Ray paths for propagating diffracted waves are defined according to a generalized Fermat principle, which is also valid by analytic continuation for evanescent diffracted ray fields. The mechanism of uniform compensation for the FW-field discontinuities (across their truncation shadow boundaries) by the diffracted waves is explored for propagating and evanescent FW's, including the cutoff transition from the propagating to the evanescent regime for both the FW and diffracted constituents. Illustrative examples demonstrate: 1) the accuracy and efficiency of the high-frequency algorithm under conditions that involve the various wave processes outlined above and 2) the cogent interpretation of the results in terms of the uniform FW-modulated GTD.

Index Terms—Electromagnetic diffraction, Green's functions, phased-array antennas.

I. Introduction

IN PART I of this paper [1], a uniform high-frequency solution is presented for the electric field $\vec{E}$ radiated at finite distance by a planar semi-infinite phased array of parallel elementary electric dipoles. The array is infinite in the z-direction and semi-infinite in the x-direction with interelement period d_x and d_z in the x and z directions, respectively; the dipoles are linearly phased with γ_x and γ_z denoting the interelement phasings

along the x and z coordinates, respectively, (see [1, Fig. 2]). The time harmonic ($e^{j\omega t}$) electric field is represented in terms of a series encompassing propagating and evanescent Floquet waves $\vec{E}_{pq}^{\text{FW}}(\vec{r})(\vec{r} \equiv (x, y, z) \equiv (\rho, \phi, z))$ together with their corresponding diffracted fields $\vec{E}_q^d(\vec{r})$, which arise from the edge of the array. Using the same notation as in [1], the high-frequency solution is summarized as

$$\vec{E}(\vec{r}) = \sum_{p, q=-\infty}^{\infty} \vec{E}_{pq}^{\text{FW}}(\vec{r}) U(\phi_{pq}^{\text{SB}} - \phi) + \sum_{q=-\infty}^{\infty} \vec{E}_q^d(\vec{r}) \quad (1)$$

where

$$\vec{E}_{pq}^{\text{FW}}(\vec{r}) = \frac{\vec{G}(k_{xp}, k_{ypq}, k_{zq})}{2 d_x d_z k_{ypq}} e^{-j(k_{xp}x + k_{ypq}y) + k_{zq}z} \quad (2)$$

represents the Floquet waves (FW) on the *infinite* array, truncated in (1) via the Heaviside unit step function $U(\eta)$ at the shadow boundary plane $\phi = \phi_{pq}^{\text{SB}}$ [1, eq. (22)]. In (1)

$$\vec{E}_q^d(\vec{r}) \sim \frac{e^{-j(k_{\rho q}\rho + k_{zq}z)}}{4\pi d_z} \sqrt{\frac{2\pi j}{k_{\rho q}\rho}} \left[\vec{D}_q(\phi)\right.$$
$$+ \sum_{p=-P}^{P} \left(\vec{w}_{pq-}(\phi)[F(\delta_{pq-}^2) - 1]\right.$$
$$\left.\left.+ \epsilon_p \vec{w}_{pq+}(\phi)[F(\delta_{pq+}^2) - 1]\right] \quad (3)\right.$$

represents edge-generated diffracted fields, which uniformly compensate for the discontinuity of the truncated FW's. The FW indexes q and p tag features associated with the array periodicities along the infinite z domain and the semi-infinite x domain, respectively. In (2), $\vec{G}(k_x, k_y, k_z)$ is the spectral amplitude of the vector electric field radiated in free-space by an elementary dipole oriented along z [1, eq. (13)], $k_{xp}, k_{zq}, k_{\rho q}, k_{ypq}$ are the propagation constants (spectral wavenumbers) of the pqth FW along the directions x, z, ρ, y, respectively (see [1, fig. 2, eqs. (7), (9), (14), (19)]), while $\alpha_{pq} = \cos^{-1}(k_{xp}/k_{\rho q})$ is the angular spectrum formulation corresponding to the (ρ, ϕ) coordinate frame ([1, eq. (18)]). Furthermore, $\vec{D}_q, \epsilon_p$ and $\vec{w}_{pq\pm}$ are defined in [1, eqs. (17), (25), and (26)] and $F(\eta)$ is the transition function of the uniform theory of diffraction (UTD) [1, eq. (29)], [2], whose arguments are $\delta_{pq\pm}^2$ defined in [1, eq. (30)]. The above formulation applies for $\phi \epsilon (0, \pi)$; expressions for $\phi \epsilon (\pi, 2\pi)$ may be obtained by formally substituting $\phi \to 2\pi - \phi$ and $y \to -y, \hat{y} \to -\hat{y}$.

The present paper deals with the phenomenology of the diffracted fields which are formally represented in (3). In Section II, ray theory is introduced to parameterize and interpret the diffracted waves associated with both propagating (radiating) and evanescent (nonradiating) truncated FW. The FW (diffracted field) connection, which is established via phase matching along the edge (z-axis), can be expressed as a Floquet-generalized Fermat principle. The diffracted fields as such are categorized in terms of propagating and radially evanescent contributions depending on whether $k_{\rho q}$ is real or imaginary. Section III deals with the mechanism of uniform compensation for the FW field discontinuities by the diffracted waves, and with the spatial transition regions near the shadow boundaries, due to propagating and evanescent FW's incident on the edge. Section IV calls attention to phenomena associated with FW cutoff on truncated arrays by tracking the high-frequency solution through the transition from the propagating to the evanescent regime. Moreover, the cutoff transition of diffracted waves from conical propagation to radial evanescence is discussed. Section V deals with simplifications of the various solutions in the far-field limit. Section VI contains illustrative examples that test the accuracy and effectiveness of our high-frequency solution, and quantify the influence of various wave processes on the solution. The paper ends with conclusions in Section VII.

II. GENERALIZED FERMAT PRINCIPLE FOR DIFFRACTED RAYS

The ray interpretation of the FW and diffracted wave solutions is based on the wavenumber vectors $\vec{k}_{pq}$ and $\vec{k}_q^d$, which parameterize the ray field. Thus, we introduce

$$\vec{k}_{pq}^{\mathrm{FW}} = k_{xp}\hat{x} + k_{ypq}\hat{y} + k_{zq}\hat{z} \qquad (4)$$

as the wave vector perpendicular to the phase front of the propagating FW's. The caret ^ denotes a unit vector. For a propagating FW (PFW), $\vec{k}_{pq}^{\mathrm{PFW}}$ is real and identifies the radiation (ray) direction of the pqth PFW (PFW$_{pq}$). For an evanescent FW (EFW), the y component of $\vec{k}_{pq}^{\mathrm{EFW}}$ is purely imaginary. The EFW's propagate at grazing with phase-propagation (ray) vector

$$\Re e(\vec{k}_{pq}^{\mathrm{EFW}}) = k_{xp}\hat{x} + k_{zq}\hat{z} \qquad (5\mathrm{a})$$

maintaining a phase speed less than the speed of light ($|\Re m(\vec{k}_{pq}^{\mathrm{EFW}})| > k$) and exhibiting exponential decay along $|y|$ with attenuation vector

$$\Im m(\vec{k}_{pq}^{\mathrm{EFW}}) = k_{ypq}\hat{y}. \qquad (5\mathrm{b})$$

The boundary between the propagating and the evanescent FW's is defined by the cutoff condition $k_{ypq} = 0$.

A. Propagating Diffracted Rays

The diffracted field phase term in (3) is generated by the saddle-point condition for the formal steepest descent path integral in [1, eq. (23)], and can be written as $k_{\rho q}\rho + k_{zq}z = \vec{k}_q^d \cdot \vec{r}$, with

$$\vec{k}_q^d = k_{\rho q}\cos\phi\hat{x} + k_{\rho q}\sin\phi\hat{y} + k_{zq}\hat{z} = k_{\rho q}\hat{\rho} + k_{zq}\hat{z} \qquad (6)$$
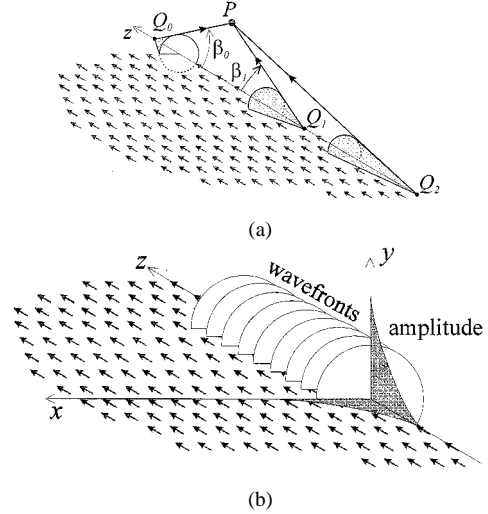

Fig. 1. Edge diffracted waves excited by FW's (3). (a) Propagating diffracted rays ($|k_{zq}| < k$) emanating from a point Q_q and propagating along a diffraction cone with aperture angle β_q. (b) Evanescent diffracted wave ($|k_{zq}| > k$) propagating along z and decaying exponentially along ρ. The wavefront and radial amplitude profile are schematized.

and $\vec{r} = \rho\cos\phi\hat{x} + \rho\sin\phi\hat{y} + z\hat{z}$. Thus, an observer at $\vec{r}$ is reached by a ray which emanates from a point Q_q at z_Q on the edge of the array with direction $\vec{k}_q^d$. Because $\vec{k}_q^d$ in the (ρ, ϕ, z) coordinate system is independent of ϕ, the phase $\vec{k}_q^d \cdot \vec{r}$ is the same for all points (ρ, z) on the ray cone centered at Q_q, with semi-angle β_q given by

$$\beta_q = \cos^{-1}\left(\frac{k_{zq}}{k}\right). \qquad (7)$$

This scenario is schematized in Fig. 1(a), which depicts the local coordinates, the ray coordinates, centered at Q_q. The ray launching mechanism is that associated with an edge-centered equivalent line source having a linear FW-based phasing $\exp(-jk_{zq}z)$, which generates the conical ray fields along $\vec{k}_q^d$ for the propagating case $|k_{zq}| < k$. This provides the connection between the FW$_{pq}$ field exciting the array edge and the resulting diffracted field, whence the point Q_q can be regarded as the FW$_{pq}$ diffraction point for the field observed at a specified $\vec{r}$. The process can also be formalized by a Floquet-generalized Fermat principle as

$$\frac{k(\vec{r} - \vec{z}_Q)}{|\vec{r} - \vec{z}_Q|} \cdot \hat{z} = \vec{k}_{pq}^{\mathrm{PFW}} \cdot \hat{z} \qquad (8\mathrm{a})$$

[see Fig. 1(a)]. Similarly, EFW's with fast phase-propagation speed along the z-axis ($|k_{zq}| < k$) diffract at a point Q_q on the edge, whose coordinate $\vec{z}_Q$ is determined by a generalized Fermat principle for EFW's

$$\frac{k(\vec{r} - \vec{z}_Q)}{|\vec{r} - \vec{z}_Q|} \cdot \hat{z} = \vec{k}_{pq}^{\mathrm{EFW}} \cdot \hat{z}. \qquad (8\mathrm{b})$$

By the previous discussion on phase matching, the projections of the phase propagation vectors for PFW's and EFW's in (8) along the z-axis are

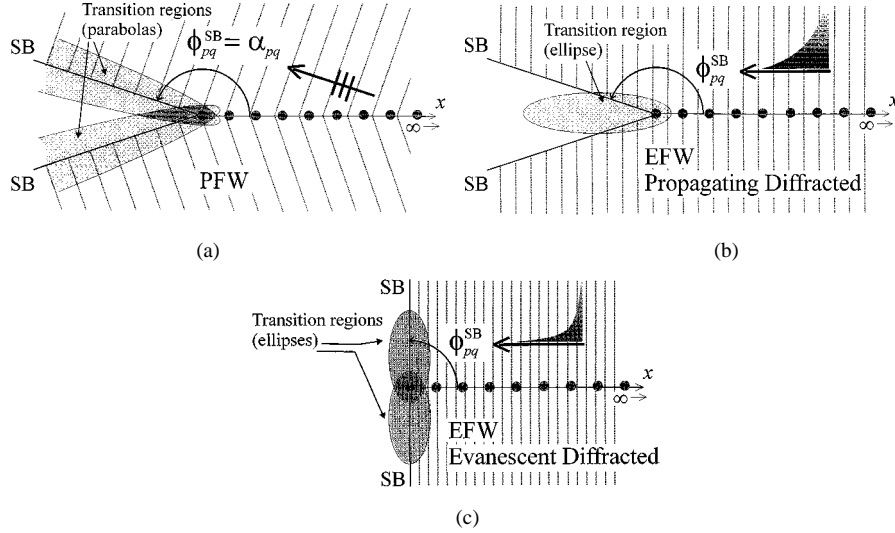$$\vec{k}_{pq}^{\substack{PFW \\ EFW}} \cdot \hat{z} = k_{zq}, \quad \text{for any } p. \qquad (9)$$

Fig. 2. z = constant plane projections of the shadow boundaries of the pqth FW and the pth transition regions of the qth diffracted ray in (3). The FW is confined to the regions $\phi < \phi_{pq}^{\mathrm{SB}}$ and $\phi > 2\pi - \phi_{pq}^{\mathrm{SB}}$. (a) PFW ($\phi_{pq}^{\mathrm{SB}} = \alpha_{pq} = \cos^{-1}(k_{xp}/k_{\rho q})$). (b) EFW, with propagating diffracted wave ($|k_{zq}| < k$; $\phi_{pq}^{\mathrm{SB}} = \cos^{-1}(k_{\rho q}/k_{xp})$). (c) EFW, with evanescent diffracted wave ($|k_{zq}| > k$; $\phi_{pq}^{\mathrm{SB}} = \pi/2$).

For this reason, the diffracted field contribution $\vec{E}_q^d(\vec{r})$ has been tagged with only one summation index q instead of the double index pertaining to the FW's. Diffracted rays produced by FW's with different k_{zq} arise from distinct diffraction points (one for each q). Moreover, far from the shadow boundaries of all FW's (ϕ far from ϕ_{pq}^{SB}), the transition function F [1, eq. (29)] tends to unity so that the summation over p in (3) does not contribute to the leading asymptotic order; what remains [i.e., the contribution associated with $\vec{D}_q(\phi)$] represents the nonuniform asymptotic expression for the diffracted field $\vec{E}_q^d(\vec{r})$. In this regime, $\vec{D}_q(\phi)$ in (3) includes all of the diffracted FW contributions denoted by $p = -\infty$ to $p = +\infty$.

B. Evanescent Diffracted Waves

As inferred from (7), the diffraction cones become more and more acute when the phase velocity of the EFW along the z-axis decreases. When k_{zq} approaches k or $-k$, the diffraction cone angle β_q tends to zero or π, respectively. After that, when $|k_{zq}| > k$, there is no real point Q_q on the edge that satisfies (8), and the solution of (7) is complex. Thus, the diffracted rays become complex and the resulting diffracted field is evanescent along the ρ direction [Fig. 1(b)], with exponential decay term

$$\vec{E}_q^d(\vec{r}) \propto e^{-|k_{\rho q}|\rho}, \qquad \text{for } q \text{ such that } |k_{zq}| > k. \quad (10)$$

The q-series of diffracted rays in (1) now converges rapidly with distance from the edge. This behavior of the diffracted waves $\vec{E}_q^d(\vec{r})$ along ρ (with q such that $|k_{zq}| > k$) could again have been anticipated because of the previously mentioned equivalence with radiation from a smooth traveling-wave line current along z, which has a phase velocity less than the speed of light. The diffracted FW's which contribute substantially to the scattered field include all PFW's and those EFW's that have $|k_{zq}| < k$. Sufficiently far away from the edge of the array,

diffraction effects caused by EFW's with $|k_{zq}| > k$ can be neglected due to their radial exponential decay.

The various asymptotic wave fields in (3) undergo spatial transitions across their respective shadow boundaries which are treated below.

III. SHADOW-BOUNDARY TRANSITION FOR DIFFRACTED WAVES

The FW shadow boundary is located where the steepest descent path (SDP) intercepts its spectral pole (see [1, Sec. III-A]). We select a FW and follow the evolution of its shadow boundary (SB) (i.e., the migration of its spectral pole) and of the corresponding diffracted field when varying the interelement phasing γ_x (this corresponds to scanning the beam of the array in the plane orthogonal to the edge). During this evolution, the FW transforms from propagating to evanescent; Fig. 2 depicts a schematic of the truncated FW in a plane orthogonal to the edge (x–y plane). Across a shadow boundary $\phi = \phi_{pq}^{\mathrm{SB}}$, the argument of the Fresnel transition function F in (3) produces a discontinuity in the representation of $\vec{E}_q^d$, which compensates for the FW truncation. Fig. 2 also shows the transition regions of $\vec{E}_q^d$, which are defined as those regions of physical space, exterior to which the diffracted field has a ray optical behavior, i.e., where the nonuniform asymptotic (isolated) evaluation of the diffracted field contribution associated with $\vec{D}_q$ in (3) is sufficiently accurate. Conversely, inside this region where the FW and diffracted ray fields cannot be separately identified the Fresnel transition function F significantly differs from unity (see Appendix), thus generating the proper transformation of the diffracted ray for uniform compensation of the truncated FW discontinuity. In the following subsections, the compensation mechanisms and the evolution of the transition regions during beam scanning are discussed for three different cases: PFW [Fig. 2(a)], EFW with propagating diffracted field [Fig. 2(b)], and EFW with evanescent diffracted field [Fig. 2(c)].
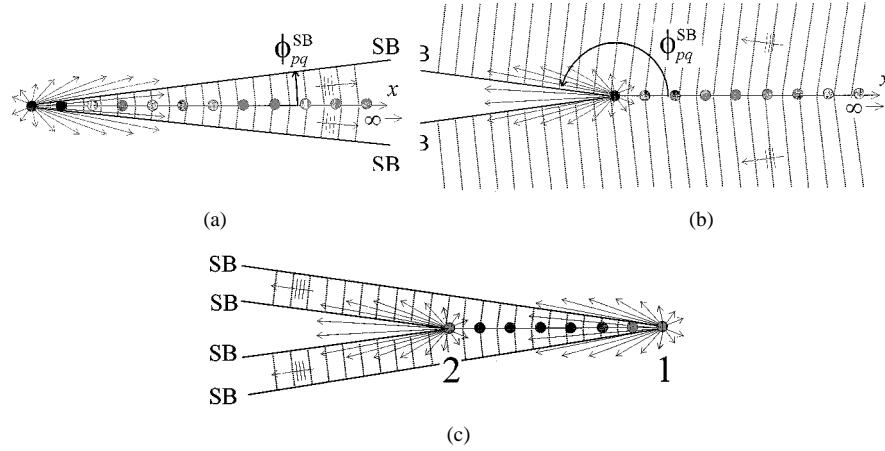
Fig. 3. Truncated FW_{pq} close to cutoff transition ($\alpha_{pq} \approx 0$ or $\approx \pi$). The amplitude of the FW tends to infinity. Longer arrows denote diffracted rays with greater amplitudes. The amplitudes of the diffracted rays tend to diverge at the shadow boundaries when these SB's approach grazing. (a) Shadow boundary close to zero ($\alpha_{pq} \approx 0$); the truncated FW for the semi-infinite array is confined to a small angular region of space. (b) Shadow boundary close to $\pi(\alpha_{pq} \approx \pi)$; the truncated FW for a semi-infinite array is distributed essentially throughout all of space. (c) Finite array close to cutoff of FW; the truncated FW is confined to a small region of space. At the cutoff limit ($\alpha_{pq} \to 0, \pi$), the angular domain of existence of the FW tends to zero and the combination of diffracted fields from the two edges provides cancellation of the singularity at grazing aspect.

A. Propagating FW's

Consider the shadow boundary ϕ_{pq}^{SB} [1, eq. (22a)] for the PFW [Fig. 2(a)], which occurs along the propagation direction of the PFW in the transverse ($z = \text{const.}$) plane

$$\phi_{pq}^{\text{SB}} = \alpha_{pq} = \cos^{-1}(k_{xp}/k_{\rho q}). \tag{11}$$

Here ($\phi \approx \phi_{pq}^{\text{SB}}$), $\delta_{pq-} = \sqrt{2k_{\rho q}\rho}\sin((\alpha_{pq} - \phi)/2)$ in [1, eq. (30)] vanishes and the uniform theory of diffraction (UTD) Fresnel function can be approximated as [2]

$$F(\delta_{pq-}^2) \approx \text{sgn}(\phi_{pq}^{\text{SB}} - \phi)\sin\left(\frac{\alpha_{pq} - \phi}{2}\right)\sqrt{2j\pi k_{\rho q}\rho} \tag{12}$$

where sgn is the sign function. Thus, the transition function F assumes the same value on each side of the SB. Consequently [see (3)]

$$F(\delta_{pq-}^2)\vec{w}_{pq-}(\phi)$$
$$\approx \text{sgn}(\phi - \phi_{pq}^{\text{SB}})\frac{\sqrt{\pi k_{\rho q}\rho}}{\sqrt{2j}k_{ypq}d_x}\vec{G}(k_{xp}, k_{ypq}, k_{zq}) \tag{13}$$

and (3) simplifies to

$$\vec{E}_q^d(\vec{r}) \sim \text{sgn}(\phi - \phi_{pq}^{\text{SB}})\frac{1}{2}\vec{E}_{pq}^{\text{FW}}(\vec{r}); \quad \phi \approx \phi_{pq}^{\text{SB}} \tag{14}$$

which states that the amplitude of the leading diffractive term in (3) is exactly 1/2 of that of the nontruncated FW field in (2) on the shadow boundary. This ensures continuity of the total scattered field. A similar behavior is known to hold for a smooth edge SB [2].

Fig. 2(a) also shows the transition region surrounding the SB. Like the transition region for the diffracted fields due to a perfectly conducting half-plane illuminated by a propagating plane wave [2], this region is cylindrical with respect to the edge and has a parabolic cross section defined by a constant value of δ_{pq-} (see (28) in Appendix).

B. Evanescent FW and Propagating Diffracted Wave

When γ_x varies such that the FW becomes evanescent [Fig. 2(b)] while maintaining a propagating diffracted field with $|k_{zq}| < k$, the shadow boundary is given by

$$\phi_{pq}^{\text{SB}} = \cos^{-1}(k_{\rho q}/k_{xp}), \quad \text{for } |k_{zq}| < k. \tag{15}$$

To interpret (15) geometrically, let us denote by $\hat{s}$ the unit vector, which defines the direction of propagation of that diffracted ray that lies exactly on the shadow boundary. This direction is identified from the intersection between the shadow boundary plane $\phi = \phi_{pq}^{\text{SB}}$ and the diffraction cone with aperture β_q

$$\hat{s} = \frac{1}{k}\vec{k}_q^d\Big|_{\phi=\phi_{pq}^{\text{SB}}} = \sin\beta_q\cos\phi_{pq}^{\text{SB}}\hat{x}$$
$$+ \sin\beta_q\sin\phi_{pq}^{\text{SB}}\hat{y} + \cos\beta_q\hat{z}. \tag{16}$$

For a PFW_{pq} [see (4) and (11)], one notes that $k\hat{s} = \vec{k}_{pq}^{\text{PFW}}$, thus confirming that the PFW_{pq} travels with the speed of light along $\hat{s}$. Although it is not obvious, the same property holds for an EFW_{pq}. In fact, (5a), (9), and (15) imply that

$$\Re e(\vec{k}_{pq}^{\text{EFW}})\cdot\hat{s} = \sin\beta_q\cos\phi_{pq}^{\text{SB}}k_{xp} + \cos\beta_q k_{zq} = k \tag{17}$$

thus demonstrating that in the direction $\hat{s}$, the phase velocity of the EFW wavefront likewise equals the speed of light. Since $\hat{s}$ lies on the diffraction cone, the entire propagating conical edge-diffracted wave travels with the speed of light. This shows that the direction where the compensation mechanism occurs, coincides with that direction which ensures the phase matching between $\vec{E}_{pq}^{\text{FW}}$ and the associated diffracted wave $\vec{E}_q^d$.

When the observer is situated near the SB ($\phi \approx \phi_{pq}^{\text{SB}}$), the argument δ_{pq-}^2 [1, eq. (28)] of the transition function $\tilde{F}$ in (3) has a vanishing real part and a nonnegative imaginary part, making

F discontinuous. Using [1, eq. (31)], the discontinuous part is put in evidence via

$$F(\delta_{pq-}^2) = 2U(\phi - \phi_{pq}^{\mathrm{SB}}) \sin\left(\frac{\alpha_{pq} - \phi}{2}\right) \sqrt{2j\pi k_{\rho q}\rho}\, e^{j\delta_{pq-}^2}$$
$$+ \sqrt{\pi}\, e^{j\pi/4}\delta_{pq-} e^{j\delta_{pq-}^2} \mathrm{erfc}(e^{j\pi/4}\delta_{pq-}) \qquad (18)$$

where

U same function as in (1);

erfc   continuous function given in [1, eq. (29)].

Introducing (18) into (3) leads to

$$\vec{E}_q^d(\vec{r}) \sim U(\phi - \phi_{pq}^{\mathrm{SB}})\vec{E}_{pq}^{\mathrm{FW}}(\vec{r}); \quad \phi \approx \phi_{pq}^{\mathrm{SB}}. \qquad (19)$$

Therefore, close to the shadow boundary, the dominant asymptotic term in $k_{\rho q}\rho$ has the same value as the nontruncated FW when $\phi > \phi_{pq}^{\mathrm{SB}}$, but vanishes when $\phi < \phi_{pq}^{\mathrm{SB}}$, thereby providing continuity of the *total* field. Note that because $\delta_{pq-}^2 = j|\delta_{pq-}^2|$, the first contribution in (18) decays exponentially, as it must in order to compensate for the EFW discontinuity. On the contrary, the second contribution in (18) is not attenuated since the function erfc asymptotically provides a term $\exp(-j\delta_{pq-}^2)$ out of a transition region. For the present case the transition region has an elliptical shape [see Fig. 2(b)]. As shown in the Appendix [see (30)] the transition ellipse has one of the two foci on the array edge and the other on the x-axis; the shadow boundary intersects the ellipse at its apex.

When γ_x changes further, the FW becomes so strongly evanescent that the shadow boundary approaches the limiting case $\phi_{pq}^{\mathrm{SB}} = \pi/2$. The transition region tends to a circle centered at the edge, as can be inferred by observing that the eccentricity $1/|\cos\alpha_{pq}|$ vanishes for $|k_{xp}| \to \infty$.

C. Evanescent FW and Evanescent Diffracted Wave

The phenomenologies in Fig. 2(a) and (b) may also be generated by variation of the interelement phasing γ_z. In that event, even the diffracted field itself may become evanescent when $|k_{zq}| > k$ [Fig. 2(c)], thus providing

$$\phi_{pq}^{\mathrm{SB}} = \pi/2, \quad |k_{zq}| > k\, (k_{\rho q}, \text{ purely imaginary}). \qquad (20)$$

The diffracted field discontinuity is described again by (19), since (18) is also valid for imaginary values of $k_{\rho q}$. As shown in the Appendix [see (31)], the transition region has again an elliptical shape but with the second focus in the y-direction. Increasing γ_z (and, thus, $|k_{zq}|$), the diffracted contribution $\vec{E}_q^d$ becomes more radially evanescent and the ellipticity of the transition regions increases as well. However, for increasing $|k_{zq}|$, $\vec{E}_q^d$ becomes insignificant due to its strong radial attenuation.

IV. Cutoff Transitions

In this section, we discuss the phenomenology of the diffracted rays for the cases in which the exciting FW's undergo transition from propagating to evanescent, as may occur during beam scanning. Furthermore, we discuss the cutoff transition

for diffracted waves from the conical propagating to the radially evanescent regime.

A. Diffracted Ray Behavior During FW Transitions

From (2), it is apparent that in each FW contribution $\vec{E}_{pq}^{\mathrm{FW}}$, a factor k_{ypq} appears in the denominator; thus, the field $\vec{E}_{pq}^{\mathrm{FW}}$ becomes singular at its cutoff condition

$$k_{ypq} = 0. \qquad (21)$$

This conditions is equivalent to

$$k^2 = k_{xp}^2 + k_{zq}^2 \qquad (22)$$

which means that the phase velocity of the FW at grazing matches the speed of light. Consequently, the fields radiated collectively by the source array superimpose coherently along the array plane, thus establishing a kind of global resonance. For the present case, since an infinite number of sources are fed by enforced currents, the field at the cut-off diverges. In actual antennas, at the beam-pointing angle where a Floquet wave is at cutoff, the active input impedances become strongly reactive, and an abrupt impedance mismatch occurs; this phenomenon is known as scan blindness.

The cutoff condition also implies that $k_{\rho q} = |k_{xp}|$. This means that the azimuthal angle α_{pq} defined by both (11) and (15) is

$$\alpha_{pq} = 0 \quad \text{or} \quad \alpha_{pq} = \pi \qquad (23\text{a, b})$$

for positive or negative k_{xp}, respectively. The two cutoff conditions in (23) describe different phenomenologies.

Consider first a situation when the pqth truncated FW approaches the condition $\alpha_{pq} = 0$ [Fig. 3(a)], thus implying from (11) that $\phi_{pq}^{\mathrm{SB}} \approx 0$. The FW just emerges from the evanescent to the propagating regime and exists in a relatively small region of space $0 < \phi < \phi_{pq}^{\mathrm{SB}} \ll 1$ and $\phi > 2\pi - \phi_{pq}^{\mathrm{SB}}$ near the array surface, as seen from (1). The first term inside the braces of the diffracted field $\vec{E}_q^d$ in (3) is finite and well behaved far from the shadow boundary. In the p-sum of (3), $w_{pq}\mp(\phi)$ contain a vanishing term $\sin\alpha_{pq}$ in the denominator [1, eq. (24)]. However, because $\epsilon_p = \mathrm{sgn}(k_{xp}) = 1$ and $\delta_{pq+}^2 \approx \delta_{pq-}^2$ the quantity

$$\vec{w}_{pq-}(\phi)F(\delta_{pq-}^2) + \epsilon_p \vec{w}_{pq+}(\phi)F(\delta_{pq+}^2) \qquad (24)$$

is finite and well behaved everywhere far from the shadow boundary. Near the shadow boundary ($\phi \approx \phi_{pq}^{SB}$), only the term in (3) that contains the relevant transition function becomes large, as it must be in order to compensate for the discontinuity of the FW as stated in (14) or (19), for PFW or EFW, respectively.

Consider now the case when the truncated FW_{pq} approaches the condition $\alpha_{pq} = \pi$, implying from (11) that $\phi_{pq}^{\mathrm{SB}} \approx \pi$. The domain of existence of this FW is all of space, as can be verified from (1) [Fig. 3(b)]. Near the cutoff condition ($\alpha_{pq} \approx \pi$), this FW exists almost everywhere with an amplitude, which tends to infinity. However, this apparently unphysical behavior does not

occur when applying the present formulation to an array of finite size, which contains a second edge. In this case indeed, the existence range of the FW is constrained to a very small angular region of space by the shadow boundary of the opposite edge of the array [Fig. 3(c)]. Now, far from the shadow boundary, the diffracted field $\vec{E}_q^d$ due to both edges is finite and well behaved; in particular, the expression in (24) when $\phi_{pq}^{\mathrm{SB}} \approx \pi$ is again finite since $\epsilon_P = -1$ and $\delta_{pq+}^2 \approx \delta_{pq-}^2$. In ray-optical terms, when $\alpha_{pq} \to 0 \ (\pi)$ and $\phi \to 0 \ (\pi)$ simultaneously, the grazing diffracted ray at edge 1 [see Fig. 3(c)], after being excited by the FW, propagates phase matched to the FW at the speed of light due to the close-to-cutoff condition. Consequently, when the same FW excites the diffracted field at edge 2, the latter is in phase with the diffracted ray from edge 1. Since the excitation coefficient at edge 2 is equal in magnitude but opposite in sign with respect to that at edge 1, the individual diffracted ray singularities cancel also for this limiting case.

B. Cutoff Transition Behavior of Diffracted Rays

The transition from propagating to evanescent diffracted rays $\vec{E}_q^d$ is defined by the cutoff condition $k_{\rho q} = 0$. From (3) one notes that the diffracted field $\vec{E}_q^d$ is singular when $k_{\rho q} = 0$ or, alternatively, when $|k_{zq}| = k \ (\beta_q = 0, \pi)$. In this limiting case, the diffraction point Q_q moves toward infinity and the aperture of the diffraction cone tends to zero or π. As already noted in connection with (7), the scattering behavior is similar to that of radiation from a traveling wave-line source whose phase velocity at cutoff is equal to the speed of light; the coherent confinement of the field energy to the vicinity of the z-axis causes the amplitude to diverge. However, the diffracted field $\vec{E}_q^d$ due to an edge of finite length is bounded by two shadow boundary cones arising from the two end-points of the edge. When $|k_{zq}| = k$, the field $\vec{E}_q^d$ again collapses to the vicinity of the edge but is radiated into space by the end-point contributions (tip diffracted fields). This will be the subject of a separate investigation.

V. FAR-FIELD LIMIT

Using the FW-modulated aperture distribution model, the far-field pattern of a strip-type array can be treated by the superposition of the nonuniform diffracted rays from the two parallel edges. For each edge, the nonuniform contribution at infinite distance from the array is given by the dominating diffractive term in (3) when the Fresnel transition function tends to unity

$$\vec{E}_q^d(\vec{r}) \sim \frac{1}{4\pi d_z} \sqrt{\frac{2\pi j}{k_{\rho q}\rho}} e^{-j(k_{\rho q}\rho + k_{zq}z)} \vec{D}_q(\phi). \quad (25)$$

The diffraction pattern $\vec{D}_q(\phi)$ contains singularities at the pth shadow boundary of the PFW_{pq} [1, eq. (17)].

For a strip array with N dipoles in the x direction, the truncated FW is confined between two parallel shadow boundary planes. On the plane orthogonal to the edges, at a distance ρ greater than $2L^2/\lambda$ (where $L = (N-1) dx$), using the far-field limit, the angular region, where each propagating FW exists

vanishes and the direct FW contribution does not contribute to the total field. The far-field pattern is then provided by the combination of the diffracted fields from the two edges, as occurs for GTD scattering by a metallic strip. In this combination, the singularities of the diffracted rays at the shadow boundaries cancel, thus providing a well-behaved field everywhere. The total far-field $\vec{E}_t(\vec{r})$ from the strip array may be obtained see [1, eq. (17)] as

$$\vec{E}_t(\vec{r}) = \frac{\sqrt{2\pi j}}{4\pi d_z} \sum_q \frac{e^{-j(k_{\rho q}\rho + k_{zq}z)}}{\sqrt{k_{\rho q}\rho}}$$
$$\cdot B_q(\phi)\vec{G}(k_{\rho q}\cos\phi, \ k_{\rho q}\sin\phi, \ k_{zq}) \quad (26)$$

where the summation over q includes only the propagating diffracted fields, $\vec{G}$ is defined in [1, eq. (13)] and

$$B_q(\phi) = \frac{1 - e^{-jNd_x[k_{\rho q}\cos\phi - \gamma_x]}}{1 - e^{jd_x[k_{\rho q}\cos\phi - \gamma_x]}} \quad (27)$$

is generated by the interference of the patterns $D_q(\phi)$ appropriate to and weighted by the initial phase at the two edges. Equation (27), which yields essentially the array factor of the FW-excited array, has maxima at $Nd_x[k_{\rho q}\cos\phi - \gamma_x] = 2p\pi$, i.e., for $\phi = \alpha_{pq}$ with α_{pq} real. This confirms the well-known connection between antenna theory and FW theory, whereby the pattern maxima line up with the SB's of the synthesizing FW's.

VI. ILLUSTRATIVE EXAMPLES

Numerical calculations have been carried out to test the accuracy and effectiveness of the asymptotic solution (1), as well as to highlight the effects of the various transitions between wave species. A reference solution is constructed via the element by element summation of the individual dipole source contributions in [1, eq. (2)], which necessarily have to be truncated. Our truncated reference arrays contain $N \times M$ elements along x and z, respectively. Because the finite array is intended to simulate the semi-infinite array of dipoles, all field evaluations are referenced to one of the z-oriented edges (the z-axis in our case) and the dimensions Nd_x and Md_z of the array should be chosen so as to render the contribution from the other edges (and therefore also from the corners) small enough to be negligible. Radial field scans are then conducted around the point $z = 0$ on the z-axis in the center of the truncated M section [see inset of Fig. 4(a)]. For one special case (the first example in Fig. 4(a) with $N = 1000$, $M = 3000$), we have successfully calibrated the asymptotics for the semi-infinite array against the reference solution because the additional edge contributions can truly be ignored from an array of this size. However, because of the excessive computation times required for this reference solution, we have chosen arrays with $N = 100$ and $M = 2000$ (Figs. 4(b) and 5) or $M = 3000$ (Figs. 6–8) for the other numerical examples (Figs. 4(b)–8). The choice $N = 100$ ensures that for observations taken along circular arcs centered at $z = 0$ on the z-axis, the field from the other z-directed edge is small in comparison but not entirely negligible. Therefore, the curves in Figs. 4(b)–8
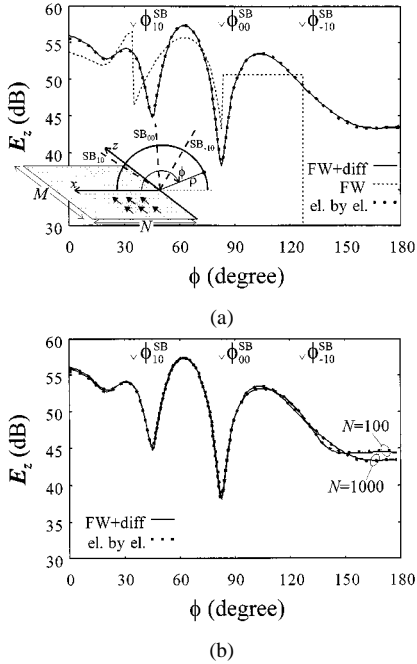
Fig. 4. Amplitude of z-component of electric field versus ϕ at radial distance $\rho = 2\lambda$ from the z-axis. $M = 3000$; $d_x = 1.4\lambda$, $d_z = 0.5\lambda$, $\gamma_x = 0.7\lambda^{-1}$, $\gamma_z = 0$ ($\vec{k}_{00}^{\text{PFW}}$ in (4) points in the direction $\beta = 90°$, $\phi = 83.6°$). Truncated FW contribution [first sum in (1)]: dashed curve; high-frequency expression of the total field in (1): solid curve; element-by-element summation: dots. (a) $N = 1000$. (b) Comparison between $N = 100$ and $N = 1000$.

calculated by our asymptotic algorithm also include the diffraction contribution from the z-edge $x = Nd_x$, thus modeling a strip array.

We now discuss these examples in detail. Fig. 4(a) shows results for a near field scan at radial distance $\rho = 2\lambda$ from the z-axis. In this example, $M = 3000$ and $N = 1000$ is chosen as noted above so as to render the contribution from the other edge negligible. The periodicity is $d_x = 1.4\lambda$, $d_z = 0.5\lambda$, and the interelement array phasing $\gamma_x = 0.7\lambda^{-1}$, $\gamma_z = 0$ is chosen so that the PFW array vector $\vec{k}_{00}^{\text{PFW}}$ in (4) points along the direction $\beta = 90°$, $\phi = 83.6°$. The three curves in Fig. 4(a) represent the z component of the electric field since all other components are zero in this case. The continuous curve is obtained by the asymptotic high-frequency solution in (1), whereas the dashed curve is obtained by the FW contributions [first summation in (1)]. The dots represent the reference solution (element-by-element summation in [1, eq. (2)]). In both cases, only a finite number of FW's $\vec{E}_{pq}^{\text{FW}}$ have been included, namely those with indexes p and q from -3 to $+3$; all others can be neglected because of their exponential decay along the y direction. Similarly, only diffracted field contributions $\vec{E}_q^d$, with index q from -3 to $+3$ are retained in the summation (1) because all others can be neglected due to their exponential decay along the ρ direction. The excellent agreement in Fig. 4(a) between the asymptotic solution in (1) and the reference solution validates the series truncations; both solutions coincide on the scale of the drawing. In fact, even a smaller number of terms would have been adequate. The periodicity $d_x = 1.4\lambda$ along the x coordinate is large enough to permit three PFW's to propagate away from the array. The propagating FW fields are $\vec{E}_{-10}^{\text{PFW}}$, $\vec{E}_{00}^{\text{PFW}}$, and $\vec{E}_{10}^{\text{PFW}}$ and their

region of existence is $\phi < \phi_{pq}^{\text{SB}}$ (see Fig. 2); the shadow boundaries SB_{pq} are here located at $\phi_{-10}^{\text{SB}} = 127°$, $\phi_{00}^{\text{SB}} = 83.6°$, and $\phi_{10}^{\text{SB}} = 34.4°$. The FW field is discontinuous at each SB, and the diffracted field $\vec{E}_0^d$, arising from the diffraction point Q_0 at $z_Q = 0$, compensates for the three discontinuities so as to provide a continuous total radiated field. Every other diffracted field $\vec{E}_q^d$ with $q \neq 0$ becomes negligible sufficiently far from the edge because of its exponential decay [see (10)]. Actually, the $q \neq 0$ diffracted fields compensate for discontinuities at the shadow boundaries of the EFW's. However, these discontinuities are small due to the EFW exponential decay along y and are practically invisible for the case in Fig. 4(a)

Fig. 4(b) compares the total field obtained from the present technique (continuous curve) for $N = 100$ and $N = 1000$; the dots again represent the reference solution. All other parameters are the same as in Fig. 4(a). For $N = 100$, the contributions from both z-edges are included. It is evident that the diffraction effect due to the far parallel edge is small compared to that of the edge under investigation. Thus, in the remaining examples, $N = 100$ will be considered sufficient to essentially highlight the effect of the diffracted field from an isolated edge, although we retain the second edge contribution in order to confirm the accuracy of the algorithm when comparing with the reference strip array.

In Fig. 5, the near-field scan is at $\rho = 2.2\lambda$ from the z-axis and the periodicity is $d_x = 0.5\lambda$, $d_z = 1.1\lambda$. The interelement array phasing $\gamma_x = -0.9\lambda^{-1}$, $\gamma_z = 0.5\lambda^{-1}$ is chosen so that the array vector $\vec{k}_{00}^{\text{PFW}}$ in (4) points along the direction $\beta = 85.4°$, $\phi = 98.3°$. The z-component of the electric field is shown in Fig. 5(a), whereas the ρ and ϕ components are shown in Fig. 5(b). The high-frequency solution [solid curve, (1)] is in excellent agreement with the reference solution (dotted curve) and significantly differs from the FW contributions alone (first summation in (1), dashed curve). As before, the FW contributions $\vec{E}_{pq}^{\text{FW}}$ and the diffracted fields $\vec{E}_q^d$ are taken over the indexes $-3 \leq (p, q) \leq 3$ because all the other FW's and diffracted waves can be neglected due to their exponential decay along the y and ρ directions, respectively. Again, excellent agreement is found between solution in (1) and the reference solution. For these parameters, three PFW's propagate away from the array: $\vec{E}_{0,-1}^{\text{PFW}}$, $\vec{E}_{00}^{\text{PFW}}$, and $\vec{E}_{01}^{\text{PFW}}$, with domains $\phi < \phi_{pq}^{\text{SB}}$ and $\phi_{0,-1}^{\text{SB}} = 105°$, $\phi_{00}^{\text{SB}} = 98.3°$, and $\phi_{01}^{\text{SB}} = 162.6°$. The FW fields are discontinuous along these directions and the diffracted fields $\vec{E}_{-1}^d$, $\vec{E}_0^d$, and $\vec{E}_1^d$ compensate for the discontinuities at $\text{SB}_{0,-1}$, SB_{00}, and SB_{01}, respectively. It is important to note that, due to the different choice of periodicity, we have three propagating diffracted fields with three different q-indexes, while in the previous example, only one propagating diffracted field ($q = 0$) occurs even though both examples have three propagating FW's. Now, the three diffracted fields arise from three different diffraction points identified as Q_{-1}, Q_0, and Q_1 in Section III-A and they propagate along three different diffraction cones with semi-angles $\beta_{-1} = 146°$, $\beta_0 = 85.4°$, and $\beta_1 = 8.6°$ given by (9) [see also Fig. 1(a)]. Every other diffracted field can be neglected sufficiently far from the truncation because of its exponential decay along ρ (this is the case here for $\rho = 2.2\lambda$). Again, as before, the diffracted field compensation for the exponentially small EFW discontinuities at their SB's
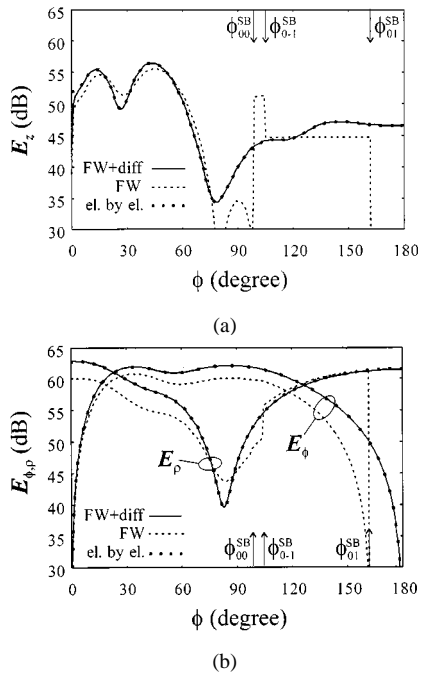
(a)

(b)

Fig. 5.   Amplitude of (a) z-component and (b) ρ- and ϕ-components of electric field versus ϕ at radial distance $\rho = 2.2\lambda$ from the z-axis. $M = 2000$, $N = 100$; $d_x = 0.5\lambda$, $d_z = 1.1\lambda$, $\gamma_x = -0.9\lambda^{-1}$, $\gamma_z = 0.5\lambda^{-1}$ ($\vec{k}_{00}^{\mathrm{PFW}}$ in (4) points in the direction $\beta = 85.4°$, $\phi = 98.3°$). FW contribution (dashed curve); FW plus diffracted field (continuous curve); element-by-element summation (dots).

cannot be detected in the plots of Fig. 5. Note that in the present case, the $q = 1$ diffracted field $\vec{E}_1^d$ is stronger than the other two due to the rather small $k_{\rho 1} = 0.94\lambda^{-1}$, which appears in the denominator of (3); the other two modes have $k_{\rho,-1} = 3.51\lambda^{-1}$ and $k_{\rho 0} = 6.28\lambda^{-1}$.

In Fig. 6, we examine a case that is almost the same as in Fig. 5. Nevertheless the difference is the now slightly smaller value of $\gamma_x = -0.945\lambda^{-1}$, which leads to quite different behavior: two propagating FW's $\vec{E}_{0,-1}^{\mathrm{PFW}}$, $\vec{E}_{00}^{\mathrm{PFW}}$, and one nonpropagating $\vec{E}_{01}^{\mathrm{EFW}}$, which decays away from the array. However, the three corresponding diffracted fields $\vec{E}_{-1}^d$, $\vec{E}_0^d$, and $\vec{E}_1^d$ all propagate away from the truncation edge. The SB's lie along $\phi_{0,-1}^{\mathrm{SB}} = 105.6°$, $\phi_{00}^{\mathrm{SB}} = 98.7°$, and $\phi_{01}^{\mathrm{SB}} = 176.5°$, respectively, and SB$_{01}$ delimits the region of existence of $\vec{E}_{01}^{\mathrm{EFW}}$ that is close to its *cutoff* condition (21)–(23); indeed, we have $k_{y01} = -j0.06\lambda^{-1}$ and $\alpha_{01} = \pi + j0.06$. At a distance $\rho = 2.2\lambda$ $\vec{E}_{01}^{\mathrm{EFW}}$ is not negligible because it is close to cutoff. At a greater distance, its contribution is negligible whereas the diffracted field $\vec{E}_1^d$ that compensates for its disappearance is propagating and, thus, cannot be ignored. In fact, $\vec{E}_1^d$ is strongest in amplitude among the three propagating diffracted FW's because $k_{\rho 1} = 0.943\lambda^{-1}$ is smaller than $k_{\rho,-1}$ and $k_{\rho 0}$. Fig. 6 highlights the important role of the diffracted field. Note that the FW contribution alone overestimates the field by about 10 dB due to the closeness of one FW to its cutoff. Under these critical conditions in which there is a quasi-grazing EFW propagating close to grazing, the diffracted field (3) compensates for the discontinuity of the EFW remarkably well and the total field predicted by (1) is in excellent agreement with the reference solution.
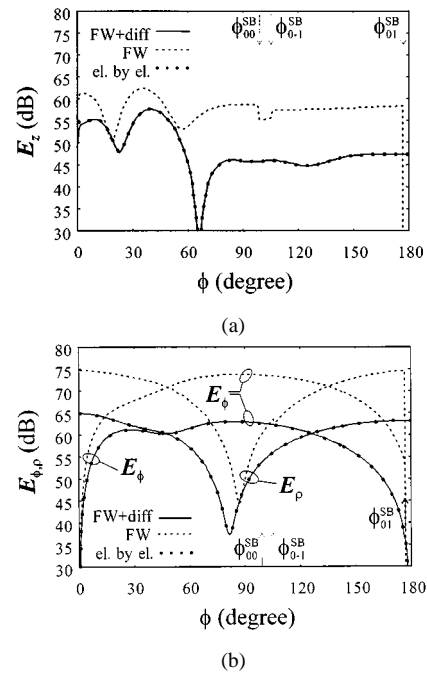

(a)

(b)

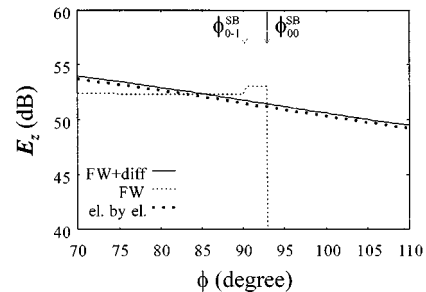Fig. 6.   As in Fig. 5, except for $\gamma_x = -0.945\lambda^{-1}$.

Fig. 7.   Amplitude of z-component of electric field versus ϕ at radial distance $\rho = 0.3\lambda$ from the z-axis. $M = 3000$, $N = 100$; $d_x = 0.5\lambda$, $d_z = 0.8\lambda$, $\gamma_x = -0.3\lambda^{-1}$, $\gamma_z = 1.57\lambda^{-1}$ ($\vec{k}_{00}^{\mathrm{PFW}}$ in (4) points in the direction $\beta = 75.5°$, $\phi = 93°$). FW contribution (dashed curve); FW plus diffracted field (continuous curve); element-by-element summation (dots).

In Fig. 7, representing the electric field z-component, the near-field scan $70° < \phi < 110°$ at $\rho = 0.3\lambda$ from the z-axis is intended to demonstrate compensation, by an evanescent diffracted field ($k_{\rho q} < k$) of an SB discontinuity due to the disappearance of an EFW contribution. The periodicity is $d_x = 0.5\lambda$, $d_z = 0.8\lambda$, with the interelement phasing $\gamma_x = -0.3\lambda^{-1}$, $\gamma_z = 1.57\lambda^{-1}$ chosen to have the array vector $\vec{k}_{00}^{\mathrm{PFW}}$ in (4) along the direction $\beta = 75.5°$, $\phi = 93°$. All designations pertaining to Figs. 4(b)–6 apply, as do the comments pertaining to the number of retained FW$_{pq}$ and diffracted contributions. Rather good agreement is found between the asymptotic solution in (1) and the reference solution, the small difference between the two curves being due to the closeness of the observation point with respect to the edge; the asymptotic evaluation loses its accuracy there. For the above parameters, only $\vec{E}_{00}^{\mathrm{PFW}}$ propagates away from the array, while $\vec{E}_{0,-1}^{\mathrm{EFW}}$ is close to its cutoff condition. Fig. 7 depicts the SB's of these two FW's, at the azimuthal angles
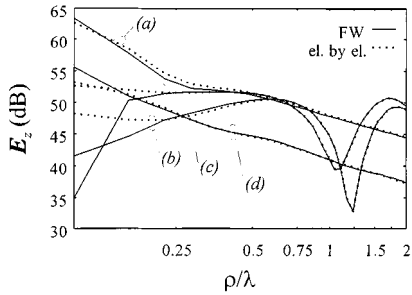
Fig. 8.   Amplitude of z-component of electric field versus ρ at $\phi = 160°$. The curves denoted by (a), (b), (c), and (d), refer to the cases treated in Figs. 4(a), and 5–7, respectively. FW plus diffracted field (continuous curve); element-by-element summation (dots).

$\phi_{0,-1}^{\mathrm{SB}} = 90°$, $\phi_{00}^{\mathrm{SB}} = 93°$, respectively. Note that $\phi_{0,-1}^{\mathrm{SB}}$ is given by (20) because $k_{\rho,-1} = -j0.1\lambda^{-1}$ is imaginary. The FW fields are discontinuous along these directions and the diffracted fields $\vec{E}_{-1}^{d}$ and $\vec{E}_{0}^{d}$ compensate for the $\mathrm{SB}_{0,-1}$ and SB_{00} discontinuities, respectively. Note that in this case the diffracted field $\vec{E}_{-1}^{d}$ is evanescent while $\vec{E}_{0}^{d}$ is propagating. Also, $\vec{E}_{-1}^{d}$ is very close to the cutoff $k_{\rho q} = 0$ for the diffracted field. The small discontinuity at $\phi = 90°$ is due to the disappearing $\vec{E}_{0,-1}^{\mathrm{EFW}}$ field and is well compensated by the evanescent diffracted field. The combination of small $\rho = 0.3\lambda$ and small $k_{y0,-1} = -j0.32\lambda^{-1}$ near the $k_{ypq} = 0$ cutoff has made it possible to highlight the compensation mechanism.

Finally, the scan along the ρ direction in Fig. 8 demonstrates the convergence of the asymptotic solution even close to the edge and close to the cutoff condition of the diffracted field. The scan is performed with ρ ranging between 0.1λ and 2λ at a fixed angle $\phi = 160°$. At greater distances, the asymptotic result in (3) is more accurate than in the proximity of the edge and its accuracy is thus not analyzed there. The four cases shown, denoted by (a), (b), (c), and (d), refer to the cases treated in Figs. 4(b)–7, respectively. Again, solid curves refer to our solution in (1), while dots refer to the reference solution. The agreement between the two solutions is fairly good even close to the edge. The solid and dotted solutions agree well for $\rho > 0.2\lambda$. Case (c) refers to the quasi-cutoff FW; nevertheless the convergence of the asymptotic solution is good even in proximity to the edge.

VII. CONCLUSIONS

In this two-part sequence of papers, we have examined the formal structure and the detailed phenomenologies pertaining to semi-infinite linearly phased planar periodic arrays of parallel current dipole radiators or, equivalently, to oblique plane wave scattering by parallel short-wire elements arranged into a planar periodic array. By collective treatment of the effects due to the individual radiators or scatterers, the problem has been rephrased in terms of a superposition of truncated FW's and the associated FW-excited edge diffractions. We have explored all possible combinations of propagating and evanescent FW-(diffracted wave) interactions and have structured the rigorous analysis in [1] in such a form as to permit efficient asymptotic eval-

uation in the high-frequency range. This formal asymptotic solution has been interpreted in the present paper (Part II) in terms of ray-optical constructs that generalize the methodology of uniform GTD for radiation from smooth linearly phased truncated plane aperture distributions to the methodology of periodicity-modulated truncated aperture distributions. Each of the generalized effects due to bulk radiation from the truncated aperture and the associated edge diffractions has been compared (where relevant) to the simpler effects encountered in the smooth conventional case. These canonical studies can now be extended to nonuniformly excited arrays. When a smooth slowly varying tapering function modifies the excitation of the elements over the entire domain of the array, the asymptotic field is modified adiabatically by invoking the local nature of high-frequency phenomena [3]. When the tapering function vanishes at the edge, significant slope diffraction contributions may arise, which are presently under investigation.

Summarizing the particulars of this paper, we have established that the periodicity-modulated diffracted rays arise from diffraction points on the edge (z-axis) and propagate from there along the surface of diffraction cones according to GTD. The aperture of these cones and the position of the diffraction points are intimately related to the z-component k_{zq} of the propagation vector associated with each exciting FW_{pq}. The diffracted waves are radially propagating or evanescent depending on whether $|k_{zq}|$ is smaller or greater than the free-space wavenumber k. Under the latter condition, the nonradiating diffracted fields behave like waves excited by an equivalent slowly phased-line current propagating along the edge, with radial decay, storing reactive energy in the vicinity of the edge dipoles. Apart from this pleasing physical interpretation of the edge-centered diffraction processes, the radially attenuated diffracted waves, which are negligible sufficiently far from the edge, furnish a simple criterion for truncating the diffracted wave series similar to that for truncating the FW series. Thus, except for calculations of fields very close to the array, our asymptotic formulation is substantially more efficient than the ordinary element by element summation (the estimated gain in computing time is about two or three orders of magnitude for the examples in Section IV). Numerical examples have demonstrated that our high-frequency algorithm is uniformly valid through a variety of shadow boundaries and cutoff transitions for the truncated FW's and their associated edge diffractions and that good accuracy prevails even relatively near the edge (down to about $\lambda/4$ in our examples).

The results obtained and the physical insight gained from this prototype problem form the basis for extension to more general truncated periodic and quasi-periodic arrays. It should be noted that the active periodic Green's function of an array of sources is the basic building block for construction of a method of moment (MoM) solution for large array antennas, which may overcome problems of large matrix inversion typical for an element-by-element approach; the field representation in terms of FW diffracted rays can be usefully employed to expand the unknown currents of the integral equation pertinent to the array problem. This leads to the hybrid asymptotic MoM method for large arrays described in [4], which is being further developed.

APPENDIX

DIFFRACTED RAY-TRANSITION REGIONS

The transition region can be analytically defined as $|F(\delta^2) - 1| > \epsilon$, where ϵ is a small arbitrarily chosen positive number. Due to the regular and continuous behavior of the transition function F in [1, eq. (29)], which tends to unity for large magnitude of its argument and vanishes for small arguments, the above relation can be equivalently expressed as $|\delta^2| < A$, where A is such that $|F(A)| \approx 1 - \epsilon$ [5]. Referring to [1, eq. (30)] and (7), this implies that

$$
\begin{aligned}
|\delta_{pq\mp}^2| &= \left| 2k_{\rho q}\rho \sin^2\left(\frac{\phi \mp \alpha_{pq}}{2}\right) \right| \\
&= k\rho|\sin\beta_q(1 - \cos\phi\cos\alpha_{pq} \mp \sin\phi\sin\alpha_{pq})| < A.
\end{aligned}
\tag{28}
$$

Since (28) does not involve the observation coordinate z, the transition regions are cylinders with axes parallel to the array edge. It can also be inferred from (28) that the two transition regions associated with $\delta_{pq\mp}$ have the same cross section and can be obtained one from the other by mirror reflection with respect to the array plane. The cross-section shape of each pair of cylinders corresponding to $\mp$ in (28) depends on the relevant FW wavenumbers.

1) Propagating FW's: In this case, both $k_{\rho q}$ and k_{ypq} are real, where both β_q and $\alpha_{pq} = \phi_{pq}^{\mathrm{SB}}$ are real. Equation (28) leads to

$$
\rho < \frac{A}{k\sin\beta_q[1 - \cos(\phi \mp \phi_{pq}^{\mathrm{SB}})]}.
\tag{29}
$$

The inequality defines the regions inside the upper (δ_{pq-}) and lower (δ_{pq+}) parabolas in Fig. 2(a), with axes along the SB's, coincident foci on the edge of the array, and vertices at a focal distance of $A/(2k\sin\beta_q)$.

2) Evanescent FW's with Propagating Diffracted Waves: In this case, $k_{\rho q}$ is still real but k_{ypq} is imaginary, where β_q is real and α_{pq} is complex (cf. [1, eq. (38) and fig. 3(a)]). Noting that $\cos\alpha_{pq}$ is real and $\sin\alpha_{pq}$ is purely imaginary, (28) is rewritten as

$$
k\rho\sin\beta_q\left[(1 - \cos\phi\cos\alpha_{pq})^2 - (\sin\phi\sin\alpha_{pq})^2\right]^{1/2} < A
\tag{30}
$$

or

$$
\rho < \frac{A}{k\sin\beta_q|\cos\alpha_{pq} - \cos\phi|}.
\tag{31}
$$

The inequality in (31) defines two coincident transition regions, which occupy the interior of an ellipse with major axis along the x-axis, one focus at the edge of the array and the other focus at distance $2A/(k\sin\beta_q|\sin\alpha_{pq}|^2)$ on the x axis; the eccentricity (the ratio between the interfocal distance and the major axis) is $1/|\cos\alpha_{pq}|$ [Fig. 2(b)]. Since $\cos\phi_{pq}^{\mathrm{SB}} = 1/\cos\alpha_{pq}$ [see (15)], the shadow boundary intersects the ellipse at the top apex [5].

3) Evanescent FW's with Evanescent Diffracted Wave: In this case, both k_{ypq} and $k_{\rho q}$ are imaginary, where both β_q and α_{pq} are complex (cf. [1, eq. (39) and fig. 3(b)]). Now, $\cos\alpha_{pq}$ is imaginary, $\sin\alpha_{pq}$ is real and greater than 1, and (28) is rewritten as

$$
k\rho|\sin\beta_q|\left[(1 \mp \sin\phi\sin\alpha_{pq})^2 - (\cos\phi\cos\alpha_{pq})^2\right]^{1/2} < A
\tag{32}
$$

or

$$
\rho < \frac{A}{k|\sin\beta_q|(\sin\alpha_{pq} \mp \sin\phi)}.
\tag{33}
$$

The transition regions are again elliptical but the major axes lie on the y-axis. One focus of each ellipse still coincides with the edge of the array; the other focus is on the relevant shadow boundary, which coincides with the positive or negative y-axis for δ_{pq-} or δ_{pq+}, respectively [Fig. 2(c)]. The interfocal distance is $2A/(k\sin\beta_q|\cos\alpha_{pq}|^2)$ and the eccentricity is $1/\sin\alpha_{pq}$.

REFERENCES

[1] F. Capolino, M. Albani, S. Maci, and L. B. Felsen, "Frequency-domain Green's function for a planar periodic semi-infinite phased array—Part I: Truncated Floquet wave formulation," *IEEE Trans. Antennas Propogat.*, pp. 67–74, this issue.
[2] R. G. Kouyoumjian and P. H. Pathak, "A uniform geometrical theory of diffraction for an edge in a perfectly conducting surface," *Proc. IEEE*, vol. 62, pp. 1448–1461, Nov. 1974.
[3] L. B. Felsen and E. Gago Ribas, "Ray theory for scattering by two-dimensional quasiperiodic plane finite arrays," *IEEE Trans. Antennas Propagat.*, vol. 44, pp. 375–382, Mar. 1996.
[4] A. Neto, S. Maci, G. Vecchi, and M. Sabbadini, "Edge fringe approach for the full-wave solution of large finite arrays," in Antennas Propagat. Soc. Symp., Montreal, Canada, submitted for publication.
[5] H. L. Bertoni, A. C. Green, and L. B. Felsen, "Shadowing on Inhomogeneous Plane Wave by an Edge," *J. Opt. Soc. Amer.*, vol. 68, no. 7, pp. 983–989, July 1978.

Filippo Capolino (S'94–M'97) was born in Florence, Italy, in 1967. He received the Laurea degree (*cum laude*) in electronic engineering and the Ph.D. degree, both from the University of Florence, Italy, in 1993 and 1997, respectively.

From 1994 to 1999 he was a regular teacher of antennas at the Diploma di Laurea, University of Siena, Italy, where he is currently a Research Associate. His research interests are in the areas of theoretical and applied electromagnetics, with a focus on high-frequency methods for electromagnetic scattering, and electromagnetic models of random surfaces.

Dr. Capolino was awarded the MMET'94 Student Paper Competition in 1994, the Raj Mittra Travel Grant for Young Scientists in 1996, and the "Barzilai" Prize for the best paper at the National Italian Congress of Electromagnetism (XI RiNEm) also in 1996. In 1997 he was a Fulbright Research Visitor in the Department of Aerospace and Mechanical Engineering at Boston University, Boston, MA. In 1998–1999 he continued his research at Boston University under a Grant from the Italian National Council for Research (CNR).

Matteo Albani (S'95) was born in Florence, Italy, in 1970. He received the Doctor degree (*cum laude*) in electronic engineering and the Ph.D. degree in electromagnetism, both from the University of Florence, Italy in 1998.

He is currently a Research Associate at the Information Engineering Department, University of Siena, Italy. His research interests are in the areas of theoretical and applied electromagnetics, in particular with high-frequency methods for the scattering and diffraction.

Dr. Albani received a special award for his Laura thesis work while at the University of Florence.

Stefano Maci (M'92–SM'99) was born in Rome, Italy in 1961. He received the Doctor degree in electronic engineering from the University of Florence, Italy, in 1987.

In 1990 he joined the Department of Electronic Engineering of the University of Florence, Italy, as an Assistant Professor. Since 1998 he has been and Associate Professor at the University of Siena, Italy. In 1997 he was an Invited Professor at the Technical University of Denmark, Copenhagen. Since 1996 he has been involved in projects of the European Space Agency regarding the electromagnetic modeling of antennas. His research interests are focused on electromagnetic scattering and diffraction. He also developed research activity on microwave antennas, particularly focused on the analysis, synthesis, and design of patch antennas.

Dr. Maci received the National Young Scientists "Francini" Award for his Laurea thesis in 1988 and the "Barziulai" Prize for the best paper at the National Italian Congress of Electromagnetism (XI RiNEm) in 1996. He is an Associate Editor of the Transactions on Electromagnetic Compatibility.

Leopold B. Felsen (S'47–A'53–M'54–SM'55–F'62–LF'90) was born in Munich, Germany, on May 7, 1924. He received the B.E.E., M.E.E., and D.E.E. degrees from the Polytechnic Institute of Brooklyn, Brooklyn, NY, in 1948, 1950, and 1952, respectively.

In 1939, he immigrated to the United States and served in the United States Army from 1943 to 1946. After 1952 he remained with the Polytechnic (now Polytechnic University), gaining the position of University Professor in 1978. From 1974 to 1978 he was Dean of Engineering. In 1994 he resigned from the full-time Polytechnic faculty and was granted the status of University Professor Emeritus. He is now Professor of Aerospace and Mechanical Engineering, and Professor of Electrical and Computer Engineering at Boston University, Boston, MA. He is the author or coauthor of over 300 papers and author or editor of several books. He is an associate editor of several professional journals and editor of the *Wave Phenomena Series* (New York: Springer-Verlag). His research interests encompass wave propagation and diffraction in complex environments and in various disciplines, high-frequency asymptotic and short-pulse techniques, and phase-space methods with and emphasis on wave-oriented data processing and imaging.

Dr. Felsen is a member of Sigma Xi and a Fellow of the Optical Society of America and the Acoustical Society of America. He has held named Visiting Professorships and Fellowships and universities in the U.S. and abroad, including the Guggenheim in 1973 and the Humboldt Foundation Senior Scientist Award in 1981. In 1974 he was an IEEE/APS Distinguished Lecturer. He was awarded the Balthasar van der Pol Gold Medal from the International Union of Radio Science (URSI) in 1975, an honorary doctorate from the Technical University of Denmark in 1979, the IEEE Heinrich Hertz Gold Medal in 1991, three Distinguished Faculty Alumnus Awards from Polytechnic University, an IEEE Centennial Medal in 1984, and the Antennas and Propagation Society Distinguished Achievement Award in 1998. Also, awards have been bestowed on several papers authored or coauthored by him. In 1977, he was elected to the U.S. National Academy of Engineering. He has served as Vice Chairman and Chairman for both the United States and the International URSI Commission B.